Improved quasiparticle self-consistent electronic band structure and excitons in β-LiGaO$_2$

Niloufar Dadkhah and Walter R. L. Lambrecht[*]

Department of Physics, Case Western Reserve University, 10900 Euclid Avenue, Cleveland, Ohio 44106-7079, USA

Dimitar Pashov

Department of Physics, King's College London, London WC2R 2LS, United Kingdom

Mark van Schilfgaarde

National Renewable Energy Laboratory, Golden, Colorado 80401, USA

The band structure of β-LiGaO$_2$ is calculated using the quasiparticle self-consistent QS$G\hat{W}$ method where the screened Coulomb interaction $\hat{W}$ is evaluated including electron-hole interaction ladder diagrams and G is the one-electron Green's function. Improved convergence compared to previous calculations leads to a significantly larger band gap of about 7.0 eV. However, exciton binding energies are found to be large and lead to an exciton gap of about 6.0 eV if also a zero-point-motion correction of about -0.4 eV is included. These results are in excellent agreement with recent experimental results on the onset of absorption. Besides the excitons observed thus far, the calculations indicate the existence of a Rydberg-like series of exciton excited states, which is however modified from the classical Wannier exciton model by the anisotropies of the material and the more complex mixing of Bloch states in the excitons resulting from the Bethe-Salpeter equation. The exciton fine structure and the exciton wave functions are visualized and analyzed in various ways.

I. INTRODUCTION

Lithium gallate (β-LiGaO$_2$) is a well-known optical material, which has recently also received interest as a potential ultrawide-band-gap semiconductor. Its crystal structure was reported by Marezio [1] and consists of a cation-ordered wurtzite-derived structure with space group $Pna2_1$. It can be grown in bulk form by the Czochralski method [2,3] or epitaxially on ZnO [4]. It has been studied in the past for its piezoelectric properties [5,6], can be alloyed with ZnO [7,8] and CuGaO$_2$ [9], and has been studied as a substrate for GaN [2,10,11]. Its heat capacity and other thermodynamic properties were studied by Weise and Neumann [12] and Neumann *et al.* [13]. Various studies were also done of its phase transitions under high pressure [14–16]. Its elastic, phonon, and piezoelectric properties were calculated using density functional theory (DFT) by Boonchun and Lambrecht [17]. Its electronic structure was calculated at the quasiparticle self-consistent (QS)GW level (where G is the one-electron Green's function and W the screened Coulomb interaction) [16,18] and earlier at the DFT level using the modified Becke-Johnson exchange-correlation [19,20] functional by Johnson *et al.* [21]. Its optical gap was obtained from absorption measurements [3,22] and a combination of x-ray absorption and emission spectroscopies [21] and found generally to be about 5.3–5.6 eV. Its native defects were recently studied [23], as well as its potential for *n*-type and *p*-type doping [24]. It was predicted that Si and Ge would be shallow donors, while Sn would be a deep donor. Doping by various diatomic molecules was also investigated but not found to lead to *p*-type doping [25]. Electron paramagnetic resonance of Li and Ga vacancies was reported by Lenyk *et al.* [26] and analyzed computationally by Skachkov *et al.* [27].

Recently, the infrared (phonon related) as well as visible ultraviolet (interband transition related) optical properties were studied with reflectivity, transmission, and spectroscopic ellipsometry by Tumėnas *et al.* [28] and indicated the existence of sharp excitons near 6.0 eV. Luminescence properties were studied by Trinkler *et al.* [29,30] and the photoluminescence excitation spectroscopy confirmed the presence of sharp free excitons near 6.0 eV. The anisotropic splitting of these excitons, reported in [30], reflects the valence band splitting, characteristic of the orthorhombic symmetry of the crystal, and is in good agreement with the recent computational study by Radha *et al.* [16]. However, the free excitons at about 6.0 eV imply a band gap significantly higher than most previous studies indicated [3,21,22]. This led us to reexamine the QSGW calculations reported in Radha *et al.* [16]. Furthermore, we here use an improved QS$G\hat{W}$ method which includes vertex corrections in the polarization, calculate the dielectric functions using the Bethe-Salpeter equation approach, and study the thus obtained excitons in some detail.

II. COMPUTATIONAL METHOD

We use here essentially the same computational method as in Radha *et al.* [16] but performed additional convergence studies and also now avoid the somewhat *ad hoc* correction of the self-energy by a factor of 80% by using the

*walter.lambrecht@case.edu

recently developed extension of the *GW* method in which the screened Coulomb interaction W is evaluated beyond the random phase approximation (RPA) by including ladder diagrams [31–33]. The QS*GW* method is based on the well-known many-body-perturbation theory of Hedin [34,35] but uses an iteration scheme where a nonlocal but Hermitian and energy-independent exchange-correlation potential $\tilde{\Sigma}$ is extracted from the *GW* self-energy $\Sigma(\omega)$, which is used to update the noninteracting Hamiltonian H^0, and its Green's function G^0 is used to calculate the self-energy $\Sigma = iGW$ of the next iteration [36]. The implementation of the method in terms of a mixed interstitial plane-wave product basis set and other technical aspects are detailed in Ref. [37], and the full-potential linearized muffin-tin-orbital (FP-LMTO) band-structure method employed and integrated with the *GW* method is fully described in Ref. [38], which describes the QUESTAAL code [39] used in this work. While electron-hole effects can also be incorporated through including an exchange-correlation kernel in the inverse dielectric function in the framework of time-dependent DFT, that approach relies on the accuracy of the kernel which typically needs to be extracted from Bethe-Salpeter-equation (BSE) calculations [40], or uses the bootstrap kernel [41]. The approach introduced by Cunningham *et al.* [31,32] instead calculates directly the four-point generalized susceptibility by solving a Bethe-Salpeter equation at each $\mathbf{q}$ point rather than only in the long-wavelength limit $\mathbf{q} \to 0$. It does so only for $W(\omega = 0)$ and within the Tamm-Dankoff approximation (TDA) but then contracts the four-point generalized susceptibility back to the two-point polarizability, $P(12) = P_{RPA}(12) - \int P_{RPA}(1134)W(34, \omega = 0)P(3422)d(34)$, needed to evaluate $W = (1 - Pv)^{-1}v$. The thus obtained improved screened Coulomb interaction is here denoted by $\hat{W}(\mathbf{q}, \omega)$. Details of the approach can also be found in [33] where it was applied to the case of LiCoO$_2$. The approach was shown to be equivalent [42,43] to including a vertex correction to the polarizability propagator extracted from the functional derivative $\delta\Sigma^{GW}/\delta G$ with Σ^{GW} the *GW* self-energy within the general Hedin set of equations. However, we clarify that no vertex corrections are included in the self-energy itself, which is justified in part by cancellations of the Z factor in $G = ZG^0 + \tilde{G}$ [37], which measures the quasiparticle versus the incoherent part ($\tilde{G}$) of the one-particle Green's function, and in the vertex which behaves as $\Gamma \to 1/Z$ in the low-frequency, $\omega \to 0$, $q \to 0$ limit. This cancellation applies whenever the noninteracting G^0 is used as opposed to the fully self-consistent G. QS*GW* and QS*GW$\hat{W}$* both make use of it, and as shown in Ref. [32] it does a remarkably good job at predicting both the band gap and ε_∞ for a wide range of materials systems. After calculating the band structure in the GGA using the PBEsol functional [44] as a starting point, QS*GW* (which becomes independent of the starting point) with W calculated in RPA, and QS*GW$\hat{W}$* with $\hat{W}$ calculated including the ladder diagrams as detailed above, we calculate the optical dielectric function following closely the usual BSE approach [45]. Specifically, we use the modified response function [46]

$$\bar{P}(1234) = P^0(1234)$$
$$+ \int d(5678)P^0(1256)K(5678)\bar{P}(7834) \quad (1)$$
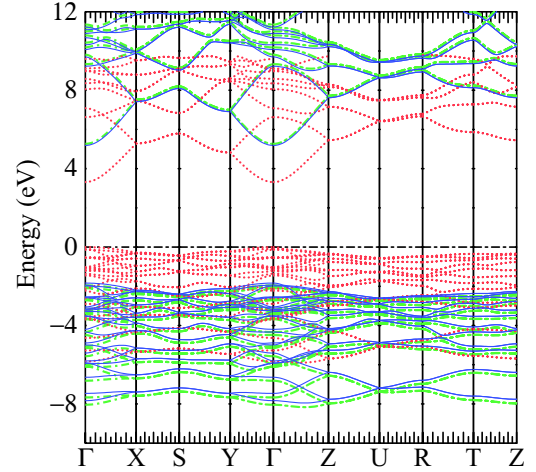
FIG. 1. Band structure of LiGaO$_2$ in the GGA (PBEsol) (red dots), QS*GW* (green dashed), and QS*GW$\hat{W}$*. The bands are all referred to the valence band maximum of the GGA band structure, thereby showing how much the gap change occurs in the valence and conduction bands separately.

with the kernel

$$K(1234) = \delta(12)(34)\bar{v} - \delta(13)\delta(24)\hat{W}(12), \quad (2)$$

with $\bar{v}_{\mathbf{G}}(\mathbf{q}) = 4\pi/|\mathbf{q} + \mathbf{G}|^2$ if $\mathbf{G} \neq 0$ and zero otherwise. The macroscopic dielectric function is then given by

$$\varepsilon_M(\omega) = 1 - \lim_{\mathbf{q} \to 0} v_{\mathbf{G}=0}(\mathbf{q})\bar{P}_{\mathbf{G}=\mathbf{G}'=0}(\mathbf{q}, \omega). \quad (3)$$

Note, that unlike the usual approach, we here use $\hat{W}$ in Eq. (2) rather than the RPA W.

III. RESULTS

A. Energy bands

In Fig. 1 we show the band structure calculated at the experimental lattice parameters in the three approaches just mentioned. We can see that using $\hat{W}$ only slightly changes the gap and mostly by shifting the valence band maximum (VBM) slightly back up compared to the down shift occurring in QS*GW* using the RPA W compared to GGA. The gaps are summarized in Table I. Our results here differ from Ref. [16]

TABLE I. Band gap of LiGaO$_2$ in different methods.

Method	E_g (eV)
PBEsol	3.31
QS*GW*	7.22
QS*GW$\hat{W}$*	7.02
QS*GW$\hat{W}$* + ZPR	6.66
PBE[a]	3.36
QS*GW*[a]	6.46
0.8Σ QS*GW*[a]	5.81
GW$_0$[b]	5.995
GW$_0$ + ZPR[b]	5.633

[a]From Rahda *et al.* [16].
[b]From Fang [47].
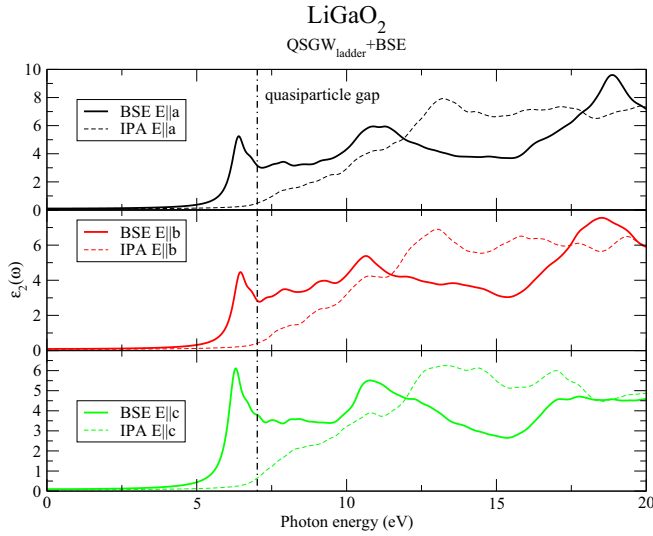
FIG. 2. Imaginary part of the macroscopic dielectric function tensor $\varepsilon_2(\omega)_{\alpha\alpha}$ for three polarizations α within the BSE and independent-particle approximation (IPA). The quasiparticle gap is indicated by the dashed line.

even for the QSGW case. We found that was due to converging the root mean square deviation of the self-energy from one iteration to the next only to a tolerance of 10^{-3} in that paper whereas now it is converged to 10^{-6}. Apparently this still affects the band gap to the order of 0.1 eV. We further tested the convergence by using a $4 \times 4 \times 4$ mesh instead of $3 \times 3 \times 3$ for the calculation of the self-energy but this was found to change the QSGW gap from 7.218 to 7.207 eV, so the $3 \times 3 \times 3$ mesh was deemed converged to ± 0.01 eV and used for the subsequent calculation of $\hat{W}$. The reduction of the self-energy shift owing to the ladder diagrams can be taken as $[E_g(QSG\hat{W}) - E_g(GGA)]/[E_g(QSGW) - E_g(GGA)]$ and amounts to 0.948, so a reduction by only $\sim 5\%$.

The zero-point motion band gap renormalization (ZPR) due to electron-phonon coupling also needs to be considered. This correction is dominated by the longitudinal optical phonon Fröhlich interaction and was estimated in Radha *et al.* [16] to be about -0.2 eV. It was recently calculated explicitly by Fang [47] to be -0.36 eV including all phonons and -0.31 eV using only the Fröhlich contribution. This author also performed GW_0 calculations and obtained a gap of 5.995 eV without and 5.633 eV with ZPR. Adding the ZPR correction to our larger gap, the quasiparticle gap is here obtained to be 6.66 eV.

B. Dielectric function and excitons

Next we calculate the macroscopic dielectric function using the BSE method. $\hat{W}$, as defined in Sec. II, is used in Eq. (2). The results are shown in Fig. 2. One can see that compared to the independent-particle approximation (where neither electron-hole nor local field effects are included) the shape of the dielectric function is strongly affected with peaks in the continuum being redshifted and a sharp exciton peak occurs below the gap for each polarization direction.
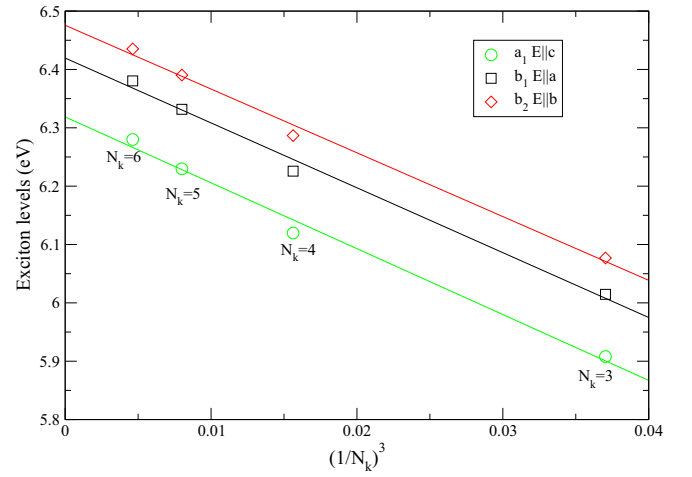
FIG. 3. Exciton band gaps for each polarization as function of **k**-mesh density.

However, to extract an accurate exciton binding energy, it is important to converge the **k**-point mesh used in the BSE two-particle Hamiltonian $H_{vc\mathbf{k},v'c'\mathbf{k}'}$ (see [32]). The results for the lowest bright exciton of each polarization as function of the inverse of the number of **k** points in the Brillouin zone are shown in Fig. 3. We here used $N_k \times N_k \times N_k$ meshes with $N_k \in \{3, 4, 5, 6\}$. We can see that the $6 \times 6 \times 6$ mesh is close to being converged and the linear extrapolation yields the values given in Table II. The line before the last line in this table gives the final exciton gaps after subtracting the ZPR correction of the gap. These values agree well with the experimental values of Trinkler *et al.* [30]. Of course, there remains some uncertainty in our calculations resulting from the extrapolations and various other approximations, such as completeness of basis set. We estimate these to be of order 0.1 eV.

The polarization dependence results from the splitting of the valence band maximum with the a_1 state (corresponding to z along **c**) forming the VBM, followed by the b_1 state (polarized along x or **a**) and b_2 (polarized along y or **b**). Our calculated splittings for these excitons are 100 meV for the a_1-b_1 splitting and 155 meV for the a_1-b_2 splitting, whereas the corresponding band splittings are 106 meV and 147 meV and the experimental splittings are 102 meV and 136 meV. The closeness of the band splittings from the exciton

TABLE II. Exciton gap convergence and comparison with experiment.

N_k	$\mathbf{E} \parallel \mathbf{c}$	$\mathbf{E} \parallel \mathbf{a}$	$\mathbf{E} \parallel \mathbf{b}$
3	5.908	6.015	6.077
4	6.120	6.226	6.287
5	6.230	6.332	6.390
6	6.280	6.380	6.435
∞	6.32	6.42	6.48
∞ + ZPR	5.96	6.06	6.12
Expt.[a]	5.931	6.033	6.067

[a]From Trinkler *et al.* [30].

TABLE III. Exciton eigenvalues ϵ_i and their polarization λ_i, oscillator strength f_i (arbitrary units), and Rydberg series quantum number n.

ϵ_i (eV)	λ_i	f_i	n
6.2800	c	502	1
6.3804	a	428	1
6.4352	b	353	1
6.6822	c	173	2
6.7824	a	149	2
6.7873		dark	2
6.8269	b	141	2
6.8328		dark	2
6.8700		dark	2
6.8773		dark	2
6.8836	c	10	3
6.8944	c	20	3
6.9026		dark	3
7.0066	a	45	3

FIG. 4. Exciton levels with their oscillator strengths for the three directions. Dark excitons indicated by crosses, placed arbitrarily in one of the three panels. The wide blue line indicates the QS$G\hat{W}$ gap.

eigenvalues indicates that the exciton binding energy is almost constant and $\sim$0.70 eV. This is a remarkably high value. In the present calculation only electronic screening is included in the exciton binding energy. While the gaps themselves were shifted by a ZPR, the $\hat{W}$ only includes electronic screening without a contribution from the lattice polarization. However, this is justified by the final binding energies being much larger than the highest phonon energies. The phonons thus are too slow to contribute to the screening of the electron-hole correlated motion in the bound exciton.

C. Exciton series analysis

Besides the lowest energy excitonic peaks discussed until now, we find a series of excited exciton states below the fundamental gap. An overview of these exciton energies and their polarization is given in Table III. From the analysis of these excitons given below, it becomes clear that these represent a modified Rydberg series.

First, their oscillator strengths show that a series of excitons with a well-defined predominant polarization exist and are associated with the top three valence band holes forming an exciton all with the same conduction band minimum (CBM) at Γ. These are shown in Fig. 4. They show a decreasing oscillator strength as we move up in the series closer to the gap. While not exactly corresponding to the hydrogenic Rydberg series where the binding energies would fall off as $1/n^2$, they approximately follow a similar series. The exciton binding energy of the ground state excitons is about 0.7 eV independent of polarization (or corresponding VB). The difference in energy to their first excited state is about 0.4 eV rather than 3/4 of 0.7 eV which would amount to 0.525 eV. For the second excited state of each polarization it is about 0.6 eV, which is rather close to 8/9 of the ground-state binding energy, which would amount to 0.62 eV. For a hydrogenic series one would expect the oscillator strengths to fall off as $1/n^3$. Here the oscillator strengths seem to fall off somewhat slower with n. We hence tentatively label these exciton series by a quantum number n corresponding to their envelope
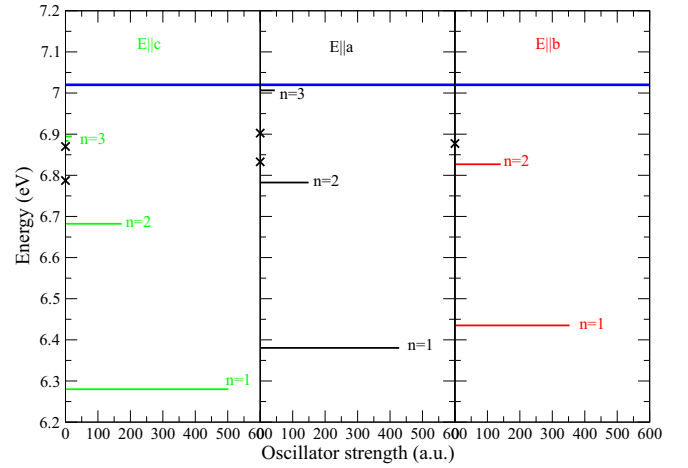
function. Besides these bright excitons with well-defined polarization, we also find several dark excitons.

There are several reasons why the hydrogenic model is not expected to apply strictly. First, the long-range screened Coulomb interaction in an anisotropic (orthorhombic) medium is given by

$$W(\mathbf{r}) = \frac{1}{\sqrt{\varepsilon_{xx}\varepsilon_{yy}\varepsilon_{zz}}} \frac{e^2}{\sqrt{\frac{x^2}{\varepsilon_{xx}} + \frac{y^2}{\varepsilon_{yy}} + \frac{z^2}{\varepsilon_{zz}}}} \qquad (4)$$

or in tensor notation $W(\mathbf{r}) = e^2/\sqrt{\det(\varepsilon)\varepsilon_{ij}^{-1}x_i x_j}$. However, the anisotropy of the dielectric constant ε_∞ is rather small, as shown by the experimental values extracted from the extrapolation of the index of refraction in the range 1–4 eV to zero frequency but not including the phonon contributions. They are $\varepsilon_{xx} = 3.027$, $\varepsilon_{yy} = 2.931$, and $\varepsilon_{zz} = 3.017$ [28].

The BSE calculations presented here also give us the real part of the electronic contribution to the macroscopic dielectric tensor $\varepsilon(\mathbf{q} \to 0, \omega = 0)$. These values are more sensitive to the accuracy of the optical matrix elements than the peak positions in the spectrum, which suffer from the difficulties in evaluating the contributions of the nonlocal self-energy $d\Sigma/dk$. The latter represents an additional term to the momentum operator $\mathbf{p}/m$ in the commutator $[\mathbf{r}, H]$ giving the velocity operator. To bypass this problem they are calculated at finite $\mathbf{q}$ and extrapolated to $\mathbf{q} \to 0$ using a model dielectric function [48] for the q dependence of the form $[\varepsilon(q) - 1]^{-1} = [\varepsilon(0) - 1]^{-1} + \alpha q^2 + \beta q^4$. This procedure using a few $\mathbf{q}$ points near $\mathbf{q} = 0$ in each direction gives $\varepsilon_{xx} = 2.90$, $\varepsilon_{yy} = 2.83$, $\varepsilon_{zz} = 2.88$, using 24 valence bands and 12 conduction bands. The results depend slightly on how we interpolate. Using a quadratic interpolation on $\varepsilon(q)$ directly gives $\varepsilon_{xx} = 2.99$, $\varepsilon_{yy} = 2.95$, $\varepsilon_{zz} = 2.96$ even closer to the experimental results. No matter which extrapolation to $q = 0$ is used, these are robustly within $\sim$2% of the experimental values, similar to the findings of Ref. [32] for a wide range of materials systems. In contrast, if we use the W without ladder diagrams in the BSE, and start from the QSGW self-energy, we find $\varepsilon_{xx} = 2.81$, $\varepsilon_{yy} = 2.75$, $\varepsilon_{zz} = 2.81$, which
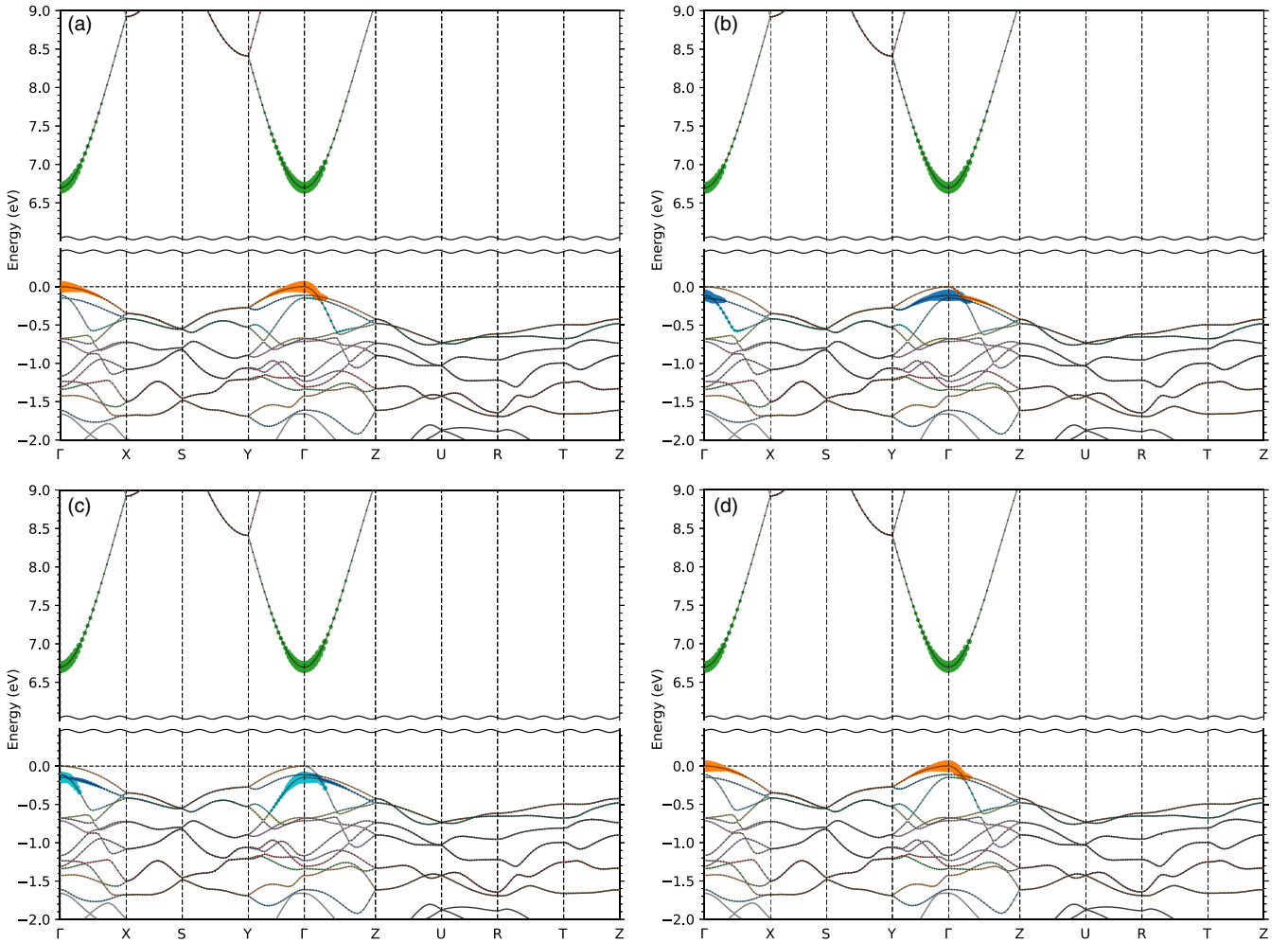
FIG. 5. Weights of exciton wave function contributed by different bands for (a)–(d) first to fourth excitons. The size of the colored circles indicates the exciton weight $|A_{vc\mathbf{k}}^{\lambda}|^2$ for a given exciton λ. The colors have no meaning and only serve to distinguish different bands.

are systematically smaller by $\sim$3% than using $\hat{W}$ indicating the underscreening of W in the standard QSGW, and which in the present material is consistent with the corresponding overestimate of the Σ or gap correction by about 5% when using W instead of $\hat{W}$. In several materials, this error in the screening is somewhat larger, of order 10%–20%. But the point is that the $\varepsilon(q \rightarrow 0, \omega = 0)$ is underestimated in the same systematic way as the Σ is overestimated. This provides another strong indication that the quasiparticle gaps obtained in the ladder approximation (QS$G\hat{W}$) include the right amount of screening. Both the peak positions of the excitons and the real parts $\varepsilon_1(0)$ agree well with experiment.

Returning to the discussion of the applicability of the hydrogenic model for the excitons, we note that the effective mass tensor is strongly anisotropic for each VB with a small effective mass of order 0.4 for the direction corresponding to the symmetry of the state, and mass of order 3.5–3.8 in the other directions. For example, for the VBM of symmetry a_1 corresponding to z, the mass is small in the z direction but large in the x, y directions. Likewise for the next two valence bands. The conduction band mass is nearly isotropic and close to 0.4 eV. So, the reduced mass is about 0.2 for the direction with the small valence band mass and about 0.4 for the other directions. The kinetic energy in the relative motion

equation of electron and hole would be $\frac{\hbar^2}{2} \frac{1}{\mu_i} \frac{\partial^2}{\partial x_i^2}$, with μ_i the reduced mass component $i = x, y, z$ and with summation convention. We thus expect excitons of a given symmetry to be somewhat more extended in the direction of the small reduced mass. Next, for excitons closer and closer to the gap, or with smaller binding energies, $\mathbf{k}$-point convergence becomes more and more challenging and requires a finer mesh. So, there are increasing errors due to the $\mathbf{k}$-mesh coarseness for higher excited state excitons. Finally, the excitons are strictly not corresponding to a single $\mathbf{k}$ point and symmetry but are a mixture of states of different $\mathbf{k}$.

D. Exciton visualization

To verify the association of the excitons with a Rydberg-like series of different envelope functions and to better understand the dark excitons, we use three different approaches. First, we analyze the excitons by considering which band-to-band transitions primarily contribute to each exciton and how these are distributed in $\mathbf{k}$ space by showing their intensity on the band structure plot. This is shown for the first four excitons in Fig. 5. In spite of the relatively high exciton binding energy, these excitons are clearly Wannier-like with the main contributions coming from the CBM near Γ and
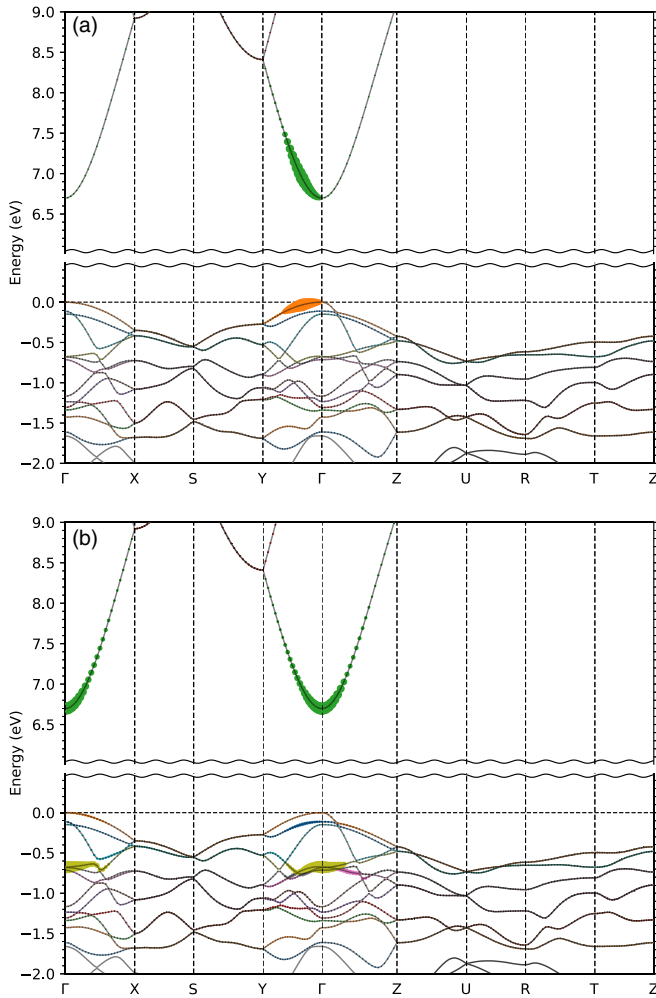
FIG. 6. Band weights of the lowest (a) and highest (b) energy dark excitons.

for excitons 1, 2, 3 the corresponding valence bands 1, 2, 3 counted from the VBM downward. The zoom-in near the VBM for the first, second, and third excitons confirms that they are coming from the top three valence bands with a_1, b_1, b_2 symmetry, respectively. One thus expects these excitons to be delocalized in real space. Similarly, we also find the fourth exciton to arise from the top valence band, which clearly identifies it as part of the Rydberg series of excitons related to this band edge. Further analysis of the **k**-space distribution is given later and shows that it has a **k**-space envelope function with a radial node whereas the first exciton has a

nodeless envelope function but in Fig. 5 this is not visible and exciton 1 and exciton 4 appear identical.

Now, looking at the dark excitons, Fig. 6 shows that the first dark exciton (at 6.7873 eV) has zero contribution from Γ and has contributions only from the top valence and lowest conduction bands but only along the Γ-Y symmetry line. This is readily explained if it is a $2p_y$-like envelope function which has a nodal plane in the x plane. While spherical symmetry does not strictly apply, as already discussed above, we can still classify the excitons according to the irreducible representations of the point group at Γ in so far as the excitons are dominated by contributions from band-to-band pairs at Γ. Thus a p_y spherical symmetry corresponds to b_2 symmetry in the C_{2v} group and is characterized by odd symmetry relative to the xz mirror plane perpendicular to y.

Similarly (not shown), the second dark exciton (at 6.8328 eV) also has contributions from the top valence band and bottom conduction band but now has a node in the y plane, so it must have a envelope function with approximately p_x spherical harmonic character, or more precisely, b_1 symmetry in the C_{2v} point group. The next dark exciton (at 6.8700 eV) has contributions from the second valence band (which has b_1 or x-like symmetry) but has contributions only along Γ-Y so it has an x-nodal plane. Finally, the highest energy dark exciton (closest to the conduction band) is shown in Fig. 6 because it has a somewhat different interesting character. One can see that here several valence bands participate. The second valence band has contributions along both Γ-X and Γ-Y but not at Γ and not along Γ-Z. We thus conclude it has a z-nodal plane in terms of these contributions. However, it also has contributions from a deeper valence band which has contributions in all three directions near Γ but is nonetheless dark because of the symmetry of this band, which we checked to be a_2 and therefore not dipole allowed.

As a second approach, the spatial extent of the excitons in real space is illustrated in Figs. 7 and 8. Here we present isosurface plots of $|\Psi^\lambda(\mathbf{r}_e, \mathbf{r}_h)|^2 = |\sum_{vc\mathbf{k}} A^\lambda_{vc\mathbf{k}} \psi_{v\mathbf{k}}(\mathbf{r}_h)\psi_{c\mathbf{k}}(\mathbf{r}_e)|^2$ for the hole position $\mathbf{r}_h$ chosen on one of the O located above a Li atom as function of the electron position $\mathbf{r}_e$. In the expansion of the one-electron eigenstates, only the smooth part of the muffin-tin orbitals represented on a real-space mesh in the unit cell is included. The calculation used a $6 \times 6 \times 6$ **k**-point mesh and hence obtains the excitons in a $6 \times 6 \times 6$ supercell. We plot these using the VESTA plotting software [49] and use an isosurface value, approximately 10% of the maximum of the function. The latter varies somewhat arbitrarily because the smooth parts of the basis functions are not normalized. To extract these real-space probabilities and the band weights
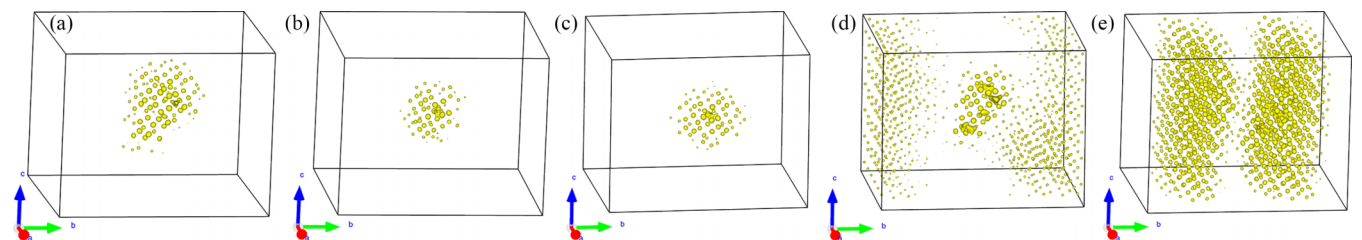
FIG. 7. Spatial distribution of excitons: the yellow isosurfaces correspond approximately to 10% of the maximum value. (a)–(d) correspond to excitons 1–4 and (e) to the exciton No. 6 in Table III, which is the first dark exciton.
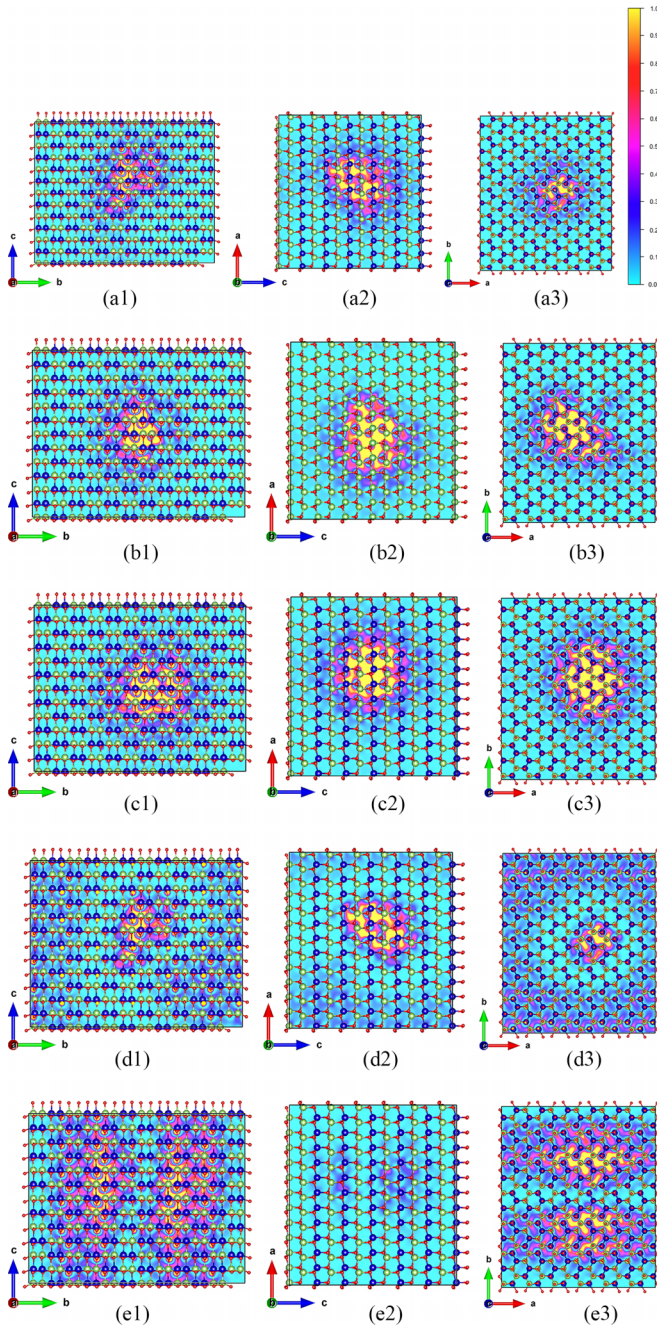
FIG. 8. Sections through the center of the excitons 1–4 and 6 (of Table III) from top to bottom and in different planes from left to right. The data values d are converted to a color index T between 0 and 1, $T = (d - S_{min})/(S_{max} - S_{min})$ with $S_{min} = 0$ and $S_{max} \approx 0.02 d_{max}$. For $d > S_{max}$ the highest color level $T = 1$ is used.

we reduced the number of bands included in the BSE calculation to only 6 valence bands and one conduction band. This slightly modifies the exciton binding energies and even how many separate excitons we obtain as eigenvalues but we can still identify the excitons with those in Table III.

Because of the 3D structure, it is impractical to superpose the structure on the isosurface plots and maintain a 3D perspective view as we do in Fig. 7. The box corresponds to a $6 \times 6 \times 6$ supercell and the hole is placed near the

center. The isosurface then shows the probability distribution of finding the electron at a level 10% of the maximum. These figures give an idea of the overall spread of the exciton and show a nonmonotonic structure in some cases. The relation of the structure to the isosurface can be better seen in Fig. 8 where we show sections in the a, b, c planes passing through the center of the distribution. Here we can still see the overall spread but in addition we can see that the probability to find the electron is larger near a few of the Ga atoms close to the hole located on an O above Li in the center of the box. One can see that the excitons 1–3 have similar spatial extent, which is consistent with them being $n = 1$ excitons corresponding to different valence bands. The isosurface value is chosen so as to show sizable contributions near the atoms. The overall size is somewhat arbitrary but clearly the excitons extend over at least 10 Å. This is consistent with an effective Bohr radius of $\hbar^2 \varepsilon / \mu e^2$ with a reduced mass of about 0.2 and dielectric constant of about 3.

For exciton No. 4 in Table III, which we claim is an $n = 2$ bright exciton related to the top valence band, we chose the isosurface value a bit smaller to show more clearly that it extends farther in space. One can see that it has a central region similar to exciton 1, then a shell of reduced intensity (corresponding to a radial node), and then a more extended tail where the contributions on each atom are significantly smaller. This is more clearly seen in Fig. 8. This is what is expected of a $2s$-like envelope function. The fact that the tail extends all the way to the edges of the $6 \times 6 \times 6$ cell may indicate that this cell does not fully capture the real-space extent of the exciton and would require a finer **k** mesh for accurate convergence.

Exciton No. 5, which is the first dark exciton in this calculation, which uses a larger number of **k** points but fewer bands, and can be identified with exciton No. 6 in Table III, shows two distinct regions with a nodal plane perpendicular to the **b** axis in between. Although we here plot only the wave function modulo squared, giving the probability density of finding the electron at a certain position from the chosen hole position in the center of the supercell, we may expect this to be an odd function as we will explicitly show below in the **k**-space plots of the real part of the $A_{vc\mathbf{k}}^\lambda$. This is also clearly seen in Fig. 8, where in the **b** plane through the center, the values are very small. Some of the other excitons become more difficult to interpret and are also deemed less well converged in terms of **k** mesh or number of bands involved, which increases as the exciton binding energies becomes smaller. They are thus not shown here.

Finally, our third approach to analyze the excitons is to look directly at the $A_{vc\mathbf{k}}^\lambda$ coefficients on a **k** mesh. We here use an $18 \times 18 \times 18$ **k** mesh but only 1 conduction band and 6 valence bands and interpolate the results to an even finer mesh. We can either inspect individual vc pairs or sum over all vc pairs for a given exciton $F^\lambda(\mathbf{k}) = \sum_{vc} A_{vc\mathbf{k}}^\lambda$ and then display this as function of **k**. First, we should note that exciton energies calculated in this way is different from that in Table III but is deemed to be better converged in **k**. Since here we wish to focus on the low-lying excitons, we think it is more important for convergence to make the **k** mesh as fine as possible at the expense of including only a few bands. Hence, we focus only on the six lowest energy excitons in
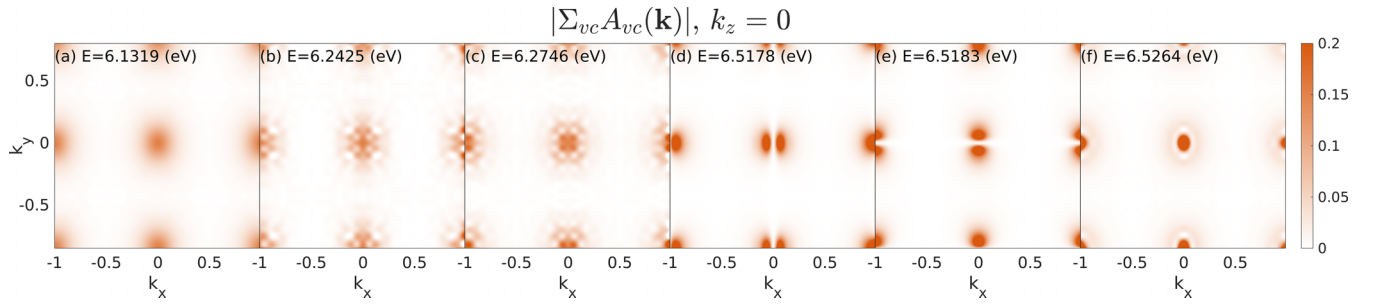
FIG. 9. Absolute value of envelope function $F^\lambda(\mathbf{k})$ for lowest six excitons calculated with an $18 \times 18 \times 18$ $\mathbf{k}$ mesh. The k_x, k_y are in units $2\pi/a$ with a the lattice constant.

the present discussion. As discussed above, in most cases only one pair contributes significantly near Γ. However, as we move away from Γ the band plots indicate that a different band number may contribute. We will see that this leads to somewhat intricate fine structure of the exciton eigenstates in $\mathbf{k}$ space. We here examine not only the absolute value but also the real and imaginary parts of these envelope functions in $\mathbf{k}$ space to evaluate their symmetry by looking for sign changes. The real and imaginary parts depend somewhat on an arbitrary phase. So, we divide the $A^\lambda_{vc\mathbf{k}}$ by a constant phase such that at the $\max_{vc\mathbf{k}} |A^\lambda_{vc\mathbf{k}}|^2$, the $A^\lambda_{vc\mathbf{k}}$ becomes purely real.

We note that the $F^\lambda(\mathbf{k})$ functions provide directly the 3D Fourier transform of the real-space exciton envelope function in a Wannier exciton model. For example for a pure spherical harmonic envelope function they would preserve the spherical harmonic character but have a radial extent in $\mathbf{k}$ space given by the spherical Hankel function transform proportional to $\tilde{f}_l(k) = \int_0^\infty f_l(r) j_l(kr) r^2 dr$ for a radial function $f_l(r)$. Similar plots of Wannier function envelope functions in $\mathbf{k}$ space were given for 2D MoS_2 by Qiu *et al.* [50], which are in-plane isotropic. However, as mentioned earlier, in the present 3D material, we do not have a pure spherical harmonic envelope function because of the anisotropy of the screened Coulomb
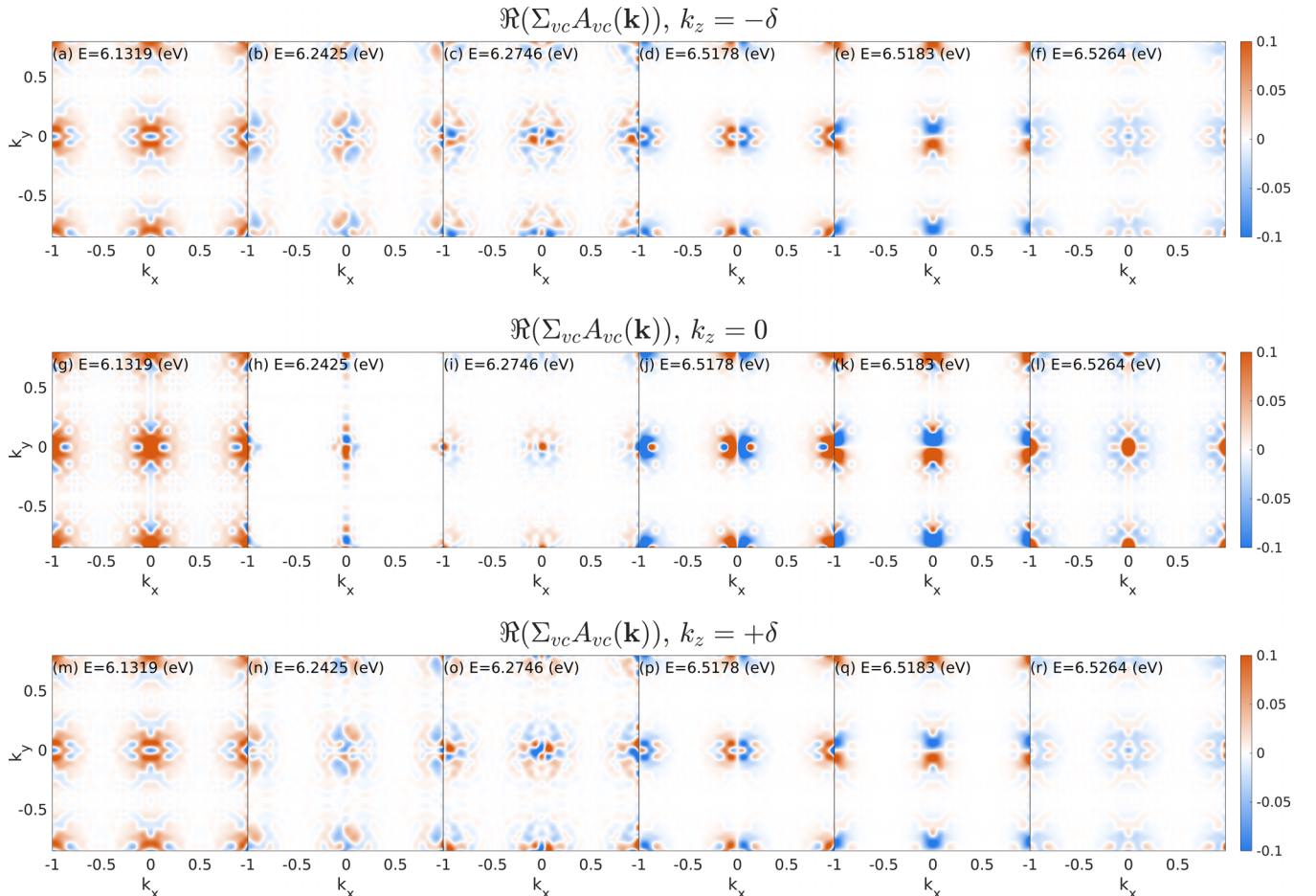
FIG. 10. Real part of the $F^\lambda(\mathbf{k})$ in three k_z planes for lowest six excitons, k_x, k_y, k_z in units of $2\pi/a$.

interaction and valence band effective masses and possibly the mixture of bands at **k** away from Γ.

Figure 9 shows the absolute value of the six lowest excitons in the $k_z = 0$ plane indicating also their eigenvalue. We can see in Fig. 9 that the first three excitons (polarized along **c**, **a**, **b**, respectively) have an envelope function with similar extent in **k** space and they show no radial nodes. In other words, they are consistent with a monotonic 1s-like function. Nonetheless, the second and third excitons are already seen to have a more intricate fine structure, which will be discussed below. Excitons 4 and 5 in this calculation turn out to be dark, and absolute value plots show they have a node in the yz and xz planes, respectively. Exciton 6 is again seen to be even but shows a radial nodal structure, which is the characteristic feature of a 2s-like exciton. The smaller inner region in **k** space indicates a larger extent in real space. The lower intensity second ring is of similar size as the envelope of the first exciton and results from the orthogonality to the lower exciton envelope function. This exciton 6 here corresponds to exciton 4 in Table III, so apparently the dark excitons 4 and 5, which are in some sense 2p-like, have actually lower energy than the 2s exciton when using a finer **k** mesh, but we can see that their energies differ by less than 0.01 eV with the two 2p dark excitons differing by less than 0.001 eV. It is thus not surprising that the order and number of excitons we obtain are quite sensitive to the **k** mesh.

The real parts are shown in Fig. 10 for all six excitons in the $k_z = 0$ and $k_z = \pm\delta k$ planes with δk the mesh spacing in the z direction. These figures clearly show that the dark excitons 4 and 5 are odd with respect to the mirror planes mentioned earlier, which explains why they are dark. A more intricate pattern of symmetries is seen in all excitons. For example for exciton 2, we can see that the function is even under a C_{2y} operation, a two fold rotation about the y axis, which changes both $k_z \rightarrow -k_z$ and $k_x \rightarrow -k_x$. It is also odd under a twofold rotation about the z axis. Although C_{2y} is not a symmetry of the crystal structure, it is a symmetry of the point group of the lattice vectors, which is D_{2h} and hence of **k** space. We can see that in the $k_z = 0$ plane it is stretched in the y direction. This is consistent with Fig. 5(c) and results from the hole mass being larger in the y than the x direction for the second band state, which has b_1 (or x-like) symmetry. This means the function will be spread out more in the x direction in real space, as can also be seen in Fig. 7(c). From Fig. 5 one can see that this exciton will also have contributions from the first and third band beyond the band crossings in **k** space. This may account for the complex superposition of different patterns. The same is true for each of these excitons. Nonetheless, one can see that the first and sixth excitons are fully a_1 symmetric. Their patterns also look quite similar at larger k but differ closer to Γ. Clearly, the Wannier exciton model based on spherical symmetry does not quite hold because of the more complex mixing of Bloch states of different **k** in the BSE theory and the anisotropies of the present system but still provides an approximate guidance to understand these excitons.

IV. CONCLUSIONS

The first conclusion of this work is that the quasiparticle band gap of β-LiGaO$_2$ calculated previously in [16] has to be

revised for three reasons. First, better self-consistency convergence of the QSGW gap increases the gap from 6.46 eV to 7.22 eV. Second, adding ladder corrections to the polarizability leads to a QS$G\hat{W}$ gap of 7.02 eV, where the self-energy is reduced by about 5% rather than the canonical 20%. Third, the electron-phonon coupling band gap renormalization estimated there was meanwhile fully calculated in [47] and gives a larger correction of -0.36 eV. Considering all these, the quasiparticle gap becomes 6.66 eV. However, exciton binding energies are found to be about 0.7 eV for the ground-state excitons related to each valence band maximum and the conduction band minimum. Taken together, this places the optical exciton gap at 5.96 eV with a dipole-allowed transition with polarization along the **c** axis, followed by a 6.06 eV exciton polarized along **a** and 6.12 eV along **b**. These results are in excellent agreement with recent spectroscopic ellipsometry [28] and photoluminescence excitation results [29,30]. These results were obtained by extrapolating the calculated exciton energies as function of the inverse of the number of **k** points in the Brillouin zone sampling to zero. Since only electronic screening is included in the BSE calculations done here, this excellent agreement with experiment suggests that indeed only electronic (as opposed to lattice) screening affects the exciton binding energy. The static real (electronic-only) dielectric constant $\varepsilon_1(\omega = 0)$ is also found to be in good agreement with experiment, suggesting that the method captures the correct amount of screening rather well by including the ladder diagrams, and that these low-order diagrams are sufficient to well capture both the one-particle Green's function and the two-particle dielectric function. The excellent agreement could be an artifact of error cancellation in the various approximations made, in particular the use of static, RPA W in the vertex for the BSE, use of the TDA, and the omission of higher order diagrams. We have made a few checks of the TDA and RPA W in several weakly correlated systems, and found the effects to be relatively small although not completely negligible. That being said, the high degree of fidelity in one- and two-particle properties for many kinds of materials and the consistency between one- and two-particle properties suggest that if results are improved by error cancellation, it is not entirely fortuitous but occurs for some reason akin to the Z-factor cancellation in the self-energy noted earlier.

Further examination of the excitons below the gap reveals that the BSE gives approximately a Rydberg-like series of excitons associated with each band edge. However, it deviates from the usual Rydberg series because of the anisotropy of the band states involved in the exciton and the Coulomb energy and the band mixing in the BSE. Several dark excitons were also found and they were shown to be associated with the same bands but with a nodal plane and therefore not fully symmetric envelope function within the point group of the system, which explains why they become dark. Rather intricate patterns of the exciton envelope functions were revealed by using a sufficiently fine **k** mesh.

[1] M. Marezio, The crystal structure of LiGaO$_2$, Acta Crystallogr. **18**, 481 (1965).

[2] T. Ishii, Y. Tazoh, and S. Miyazawa, Single-crystal growth of LiGaO$_2$ for a substrate of GaN thin films, J. Cryst. Growth **186**, 409 (1998).

[3] C. Chen, C.-A. Li, S.-H. Yu, and M. M. Chou, Growth and characterization of β-LiGaO$_2$ single crystal, J. Cryst. Growth **402**, 325 (2014).

[4] I. Ohkubo, C. Hirose, K. Tamura, J. Nishii, H. Saito, H. Koinuma, P. Ahemt, T. Chikyow, T. Ishii, S. Miyazawa, Y. Segawa, T. Fukumura, and M. Kawasaki, Heteroepitaxial growth of β-LiGaO$_2$ thin films on ZnO, J. Appl. Phys. **92**, 5587 (2002).

[5] S. Nanamatsu, K. Doi, and M. Takahashi, Piezoelectric, elastic and dielectric properties of LiGaO$_2$, Jpn. J. Appl. Phys. **11**, 816 (1972).

[6] S. N. Gupta, J. F. Vetelino, V. B. Jipson, and J. C. Field, Surface acoustic wave properties of lithium gallium oxide, J. Appl. Phys. **47**, 858 (1976).

[7] T. Omata, K. Tanaka, A. Tazuke, K. Nose, and S. Otsuka-Yao-Matsuo, Wide band gap semiconductor alloy: x(LiGaO$_2$)$_{1/2}$-$(1-x)$ZnO, J. Appl. Phys. **103**, 083706 (2008).

[8] T. Omata, M. Kita, K. Nose, K. Tachibana, and S. Otsuka-Yao-Matsuo, Zn$_2$LiGaO$_4$, wurtzite-derived wide band gap oxide, Jpn. J. Appl. Phys. **50**, 031102 (2011).

[9] I. Suzuki, Y. Mizuno, and T. Omata, Tunable direct band gap of β-CuGaO$_2$ and β-LiGaO$_2$ solid solutions in the full visible range, Inorg. Chem. **58**, 4262 (2019).

[10] A. Christensen, W. A. Doolittle, and S. Graham, Heat dissipation in high-power GaN electronics on thermally resistive substrates, IEEE Trans. Electron Devices **52**, 1683 (2005).

[11] W. A. Doolittle, T. Kropewnicki, C. Carter-Coman, S. Stock, P. Kohl, N. M. Jokerst, R. A. Metzger, S. Kang, K. K. Lee, G. May, and A. S. Brown, Growth of GaN on lithium gallate substrates for development of a GaN thin compliant substrate, J. Vac. Sci. Technol. B **16**, 1300 (1998).

[12] S. Weise and H. Neumann, Thermal analysis of LiGaO$_2$ and NaGaO$_2$, Cryst. Res. Technol. **31**, 659 (1996).

[13] H. Neumann, G. Kühn, H. Neels, E. Nowak, and E. Pirl, Heat capacity and thermodynamic properties of LiGaO$_2$ from 180 to 700 K, Cryst. Res. Technol. **22**, 413 (1987).

[14] L. Lei, T. Irifune, T. Shinmei, H. Ohfuji, and L. Fang, Cation order-disorder phase transitions in LiGaO$_2$: Observation of the pathways of ternary wurtzite under high pressure, J. Appl. Phys. **108**, 083531 (2010).

[15] L. Lei, H. Ohfuji, J. Qin, X. Zhang, F. Wang, and T. Irifune, High-pressure Raman spectroscopy study of LiGaO$_2$, Solid State Commun. **164**, 6 (2013).

[16] S. K. Radha, A. Ratnaparkhe, and W. R. L. Lambrecht, Quasiparticle self-consistent *GW* band structures and high-pressure phase transitions of LiGaO$_2$ and NaGaO$_2$, Phys. Rev. B **103**, 045201 (2021).

[17] A. Boonchun and W. R. L. Lambrecht, First-principles study of the elasticity, piezoelectricity, and vibrational modes in LiGaO$_2$ compared with ZnO and GaN, Phys. Rev. B **81**, 235214 (2010).

[18] A. Boonchun and W. R. L. Lambrecht, Electronic structure, doping, and lattice dynamics of LiGaO$_2$, in *Oxide-Based Materials and Devices II*, Proc. SPIE, Vol. 7940, edited by F. H. Terani, D. C. Look, and D. J. Rogers (SPIE, 2011), pp. 129–134.

[19] A. D. Becke and E. R. Johnson, A simple effective potential for exchange, J. Chem. Phys. **124**, 221101 (2006).

[20] F. Tran and P. Blaha, Accurate Band Gaps of Semiconductors and Insulators with a Semilocal Exchange-Correlation Potential, Phys. Rev. Lett. **102**, 226401 (2009).

[21] N. W. Johnson, J. A. McLeod, and A. Moewes, The electronic structure of lithium metagallate, J. Phys.: Condens. Matter **23**, 445501 (2011).

[22] J. T. Wolan and G. B. Hoflund, Chemical alteration of the native oxide layer on LiGaO$_2$ (001) by exposure to hyperthermal atomic hydrogen, J. Vac. Sci. Technol. A **16**, 3414 (1998).

[23] A. Boonchun, K. Dabsamut, and W. R. L. Lambrecht, First-principles study of point defects in LiGaO$_2$, J. Appl. Phys. **126**, 155703 (2019).

[24] K. Dabsamut, A. Boonchun, and W. R. L. Lambrecht, First-principles study of n- and p-type doping opportunities in LiGaO$_2$, J. Phys. D **53**, 274002 (2020).

[25] K. Dabsamut, A. Boonchun, and W. R. L. Lambrecht, N$_2$, NO, and O$_2$ molecules in LiGaO$_2$ in both Ga and Li sites and their relation to the vacancies, J. Appl. Phys. **131**, 145705 (2022).

[26] C. A. Lenyk, M. S. Holston, B. E. Kananen, L. E. Halliburton, and N. C. Giles, Lithium and gallium vacancies in LiGaO$_2$ crystals, J. Appl. Phys. **124**, 135702 (2018).

[27] D. Skachkov, W. R. L. Lambrecht, K. Dabsamut, and A. Boonchun, Computational study of electron paramagnetic resonance spectra for Li and Ga vacancies in LiGaO$_2$, J. Phys. D **53**, 17LT01 (2020).

[28] S. Tumėnas, P. Mackonis, R. Nedzinskas, L. Trinkler, B. Berzina, V. Korsaks, L. Chang, and M. Chou, Optical properties of lithium gallium oxide, Appl. Surf. Sci. **421**, 837 (2017).

[29] L. Trinkler, A. Trukhin, B. Berzina, V. Korsaks, P. Ščajev, R. Nedzinskas, S. Tumėnas, M. Chou, L. Chang, and C.-A. Li, Luminescence properties of LiGaO$_2$ crystal, Opt. Mater. (Amsterdam) **69**, 449 (2017).

[30] L. Trinkler, V. Pankratov, A. Trukhin, B. Berzina, M. Chou, and L. Chang, Anisotropic photoluminescence of β-LiGaO$_2$ crystal, Opt. Mater. (Amsterdam) **132**, 112856 (2022).

[31] B. Cunningham, M. Grüning, P. Azarhoosh, D. Pashov, and M. van Schilfgaarde, Effect of ladder diagrams on optical absorption spectra in a quasiparticle self-consistent *GW* framework, Phys. Rev. Mater. **2**, 034603 (2018).

[32] B. Cunningham, M. Gruening, D. Pashov, and M. van Schilfgaarde, QS$G\hat{W}$: Quasiparticle self-consistent *GW* with ladder diagrams in *W*, arXiv:2302.06325.

[33] S. K. Radha, W. R. L. Lambrecht, B. Cunningham, M. Grüning, D. Pashov, and M. van Schilfgaarde, Optical response and band structure of LiCoO$_2$ including electron-hole interaction effects, Phys. Rev. B **104**, 115120 (2021).

[34] L. Hedin, New method for calculating the one-particle Green's function with application to the electron-gas problem, Phys. Rev. **139**, A796 (1965).

[35] L. Hedin and S. Lundqvist, Effects of electron-electron and electron-phonon interactions on the one-electron states of solids, in *Solid State Physics*, Vol. 23, edited by F. Seitz, D. Turnbull, and H. Ehrenreich (Academic Press, New York, 1969), pp. 1–181.

[36] M. van Schilfgaarde, T. Kotani, and S. Faleev, Quasiparticle Self-Consistent *GW* Theory, Phys. Rev. Lett. **96**, 226402 (2006).

[37] T. Kotani, M. van Schilfgaarde, and S. V. Faleev, Quasiparticle self-consistent *GW* method: A basis for the independent-particle approximation, Phys. Rev. B **76**, 165106 (2007).

[38] D. Pashov, S. Acharya, W. R. Lambrecht, J. Jackson, K. D. Belashchenko, A. Chantis, F. Jamet, and M. van Schilfgaarde, Questaal: A package of electronic structure methods based on the linear muffin-tin orbital technique, Comput. Phys. Commun. **249**, 107065 (2019).

[39] See http://www.questaal.org.

[40] M. Shishkin, M. Marsman, and G. Kresse, Accurate Quasiparticle Spectra from Self-Consistent *GW* Calculations with Vertex Corrections, Phys. Rev. Lett. **99**, 246403 (2007).

[41] W. Chen and A. Pasquarello, Accurate band gaps of extended systems via efficient vertex corrections in *GW*, Phys. Rev. B **92**, 041115(R) (2015).

[42] R. Starke and G. Kresse, Self-consistent Green function equations and the hierarchy of approximations for the four-point propagator, Phys. Rev. B **85**, 075119 (2012).

[43] E. Maggio and G. Kresse, GW Vertex Corrected Calculations for Molecular Systems, J. Chem. Theory Comput. **13**, 4765 (2017).

[44] J. P. Perdew, A. Ruzsinszky, G. I. Csonka, O. A. Vydrov, G. E. Scuseria, L. A. Constantin, X. Zhou, and K. Burke, Restoring the Density-Gradient Expansion for Exchange in Solids and Surfaces, Phys. Rev. Lett. **100**, 136406 (2008).

[45] G. Onida, L. Reining, and A. Rubio, Electronic excitations: Density-functional versus many-body Green's-function approaches, Rev. Mod. Phys. **74**, 601 (2002).

[46] W. Hanke, Dielectric theory of elementary excitations in crystals, Adv. Phys. **27**, 287 (1978).

[47] D. Fang, First-principles study of the band gap renormalization and optical property of β-LiGaO$_2$, arXiv:2212.00957.

[48] G. Cappellini, R. Del Sole, L. Reining, and F. Bechstedt, Model dielectric function for semiconductors, Phys. Rev. B **47**, 9892 (1993).

[49] See https://jp-minerals.org/en.

[50] D. Y. Qiu, F. H. da Jornada, and S. G. Louie, Screening and many-body effects in two-dimensional crystals: Monolayer MoS$_2$, Phys. Rev. B **93**, 235435 (2016).